Identification of a Structurally Dynamic Domain for Oligomer Formation in Rootletin

Donghee Ko†, Jeesoo Kim†, Kunsoo Rhee and Hee-Jung Choi

Department of Biological Sciences, *Seoul National University, Seoul 08826, Republic of Korea*

Correspondence to Kunsoo Rhee and Hee-Jung Choi: *rheek@snu.ac.kr, choihj@snu.ac.kr*
https://doi.org/10.1016/j.jmb.2020.04.012
Edited by James Sellers

Abstract

Rootletin is the main component of the ciliary rootlet and functions as a centriole linker connecting the two mother centrioles. Despite the functional importance of rootletin, the molecular architecture of the rootletin filament and its assembly mechanism are poorly understood. Here, we identify the coiled-coil domain 3 (CCD3) of rootletin as the key domain for its cellular function. The crystal structure of the $CCD3^{1108–1317}$ fragment containing 28 heptad repeats and 1 hendecad repeat reveals that it forms a parallel coiled-coil dimer spanning approximately 300 Å in length. Crosslinking experiments and biophysical analyses of the minimal functional region of CCD3 (CCD3–6) suggest that CCD3–6 is structurally dynamic and may be important for oligomer formation. We also show that oligomerization-defective CCD3 mutants fail in centrosomal localization and centriole linkage, suggesting that rootletin oligomerization may be important for its function.

Introduction

The centrosome consists of a pair of centrioles surrounded by a protein matrix called pericentriolar material (PCM). A daughter centriole is attached to the mother centriole at a perpendicular angle and remains engaged until mitosis [1,2]. At the end of mitosis, the daughter centriole is disengaged from the mother centriole and becomes a young mother centriole, which recruits its own PCM to form a centrosome in a daughter cell [3]. In the early G1 phase, the young and old mother centrioles are linked by an inter-centriolar linker that places a pair of centrosomes within a close distance throughout interphase [4,5]. When a cell is about to start mitosis, the inter-centriolar linkage breaks down so that the two centrosomes are separated and function as spindle poles to pull a set of chromosomes into daughter cells [5,6].

Rootletin is the main building block of the inter-centriolar linkage [7,8]. Additional proteins, such as CEP68, CEP215, centlein, CCDC102B, LRRC45, and β-catenin are known to be associated with this linkage [9–13]. C-NAP1, another important component of the inter-centriolar linkage, is located at the proximal end of centrioles and provides a docking site for the linker proteins [14,15]. How the centriole linkers are assembled from two mother centrioles in G1 phase is not yet clear. This linker is disassembled in G2 phase by NIMA (never in mitosis A)-related kinase2 (NEK2) [16]. NEK2 phosphorylates linker proteins, such as rootletin and C-NAP1, resulting in breakage of the inter-centriolar linkage [7,14,17]. Since timely centrosome separation is crucial for the accurate segregation of chromosomes [18], highly regulated dynamics of the centriole linkage is important for cellular function.

In many cell types, including neurons and photoreceptor cells, cilia function as sensory organelles [19,20]. Through genetic analyses of rootletin mutants, rootletin has been shown to play an important role in maintaining cilium structure and function. In rootletin mutant mice, some of the ciliary structures, such as photoreceptors, degenerate over time with a striking fragility at the ciliary base [21]. In *Drosophila* Root mutant, neurons lack rootlets and have dramatically impaired sensory function, resulting in behavioral defects associated with mechanosensation and chemosensation [22,23]. In *Caenorhabditis elegans*, primary cilia of the rootletin mutants degenerate over

time due to inefficient delivery of ciliary components [24].

Human rootletin consists of 2017 amino acids and contains coiled-coil domains (CCDs). Immunostaining analyses revealed that rootletin forms fibers, which connect two centrosomes in tissue culture cells [7,17]. Fibrous structure formation of rootletin is assisted by other linker proteins, including CCDC102B and CEP68

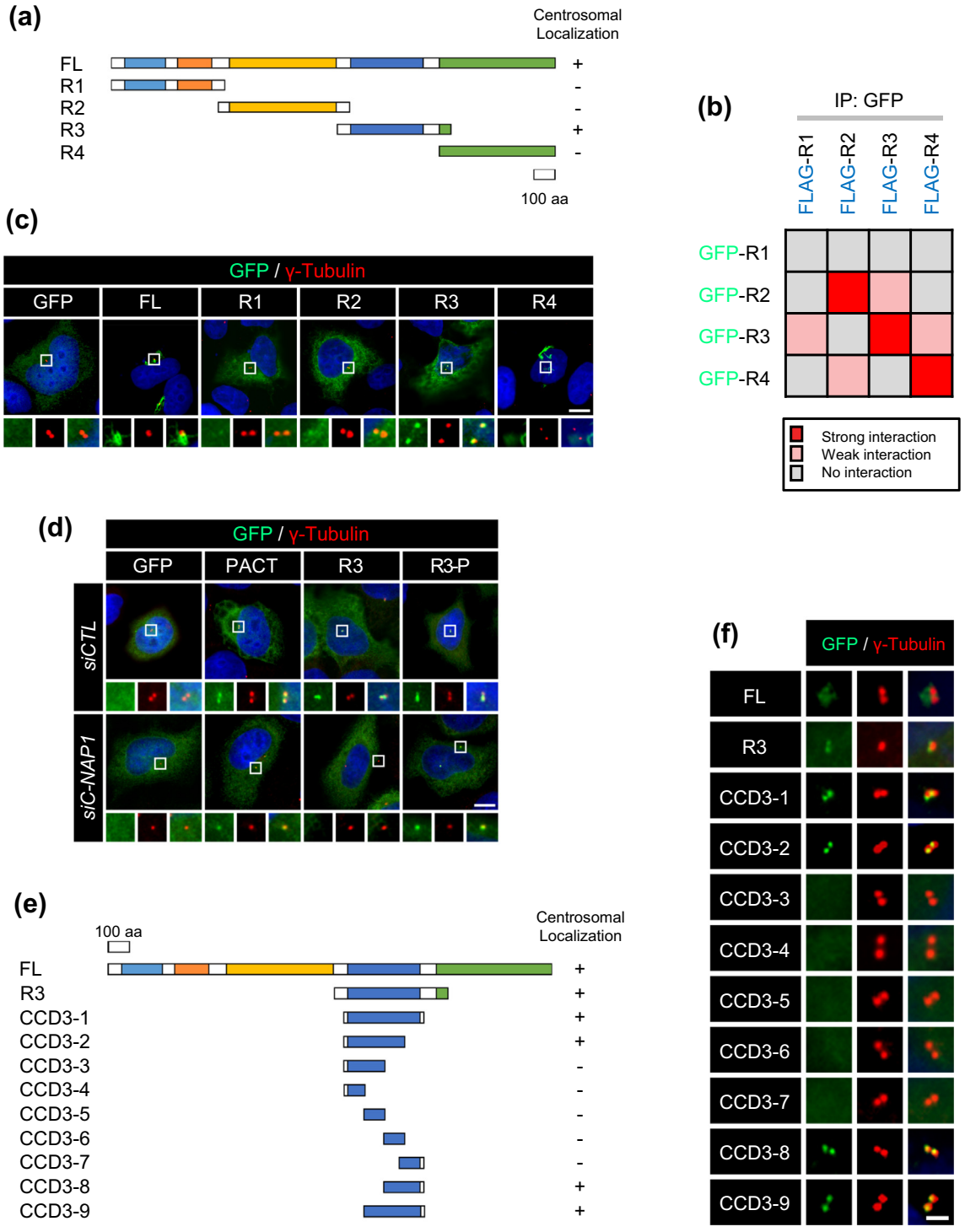

Figure 1 (*legend on next page*)

[8,11]. Recently, Schiebel and colleagues used stimulated emission depletion (STED) microscopy to observe striated patterns for rootletin and CEP68 in retinal pigmented epithelial (RPE)-1 cells [8]. The rootletin filaments form an extended, web-like network that spreads up to 1–2 μm outward from the C-NAP1 ring at the proximal ends of both centrioles [8]. The rootletin filaments coming from opposite centrioles are woven into each other, which is likely the basis of centrosome linkage [8].

Although the overall structure of the rootletin filament has been elucidated through microscopic observations, the molecular architecture of rootletin as a building unit for the intercentriolar linker and rootlet filaments remains unclear. Here, we present cell biological, biochemical, and structural studies on rootletin. In this study, we defined coiled-coil domain 3 (CCD3) as the functional domain responsible for centrosomal localization and centriole linkage and determined the crystal structures of two CCD3 dimer fragments at 1.3 and 2.8 Å resolution, respectively. Taken together with biochemical studies, our findings emphasize the functional importance of rootletin CCD3 oligomers and suggest the assembly mechanism of rootletin CCD3 at the molecular level.

Results

Domain dissection and characterization of rootletin

Rootletin was divided into four fragments (R1, R2, R3, and R4) based on previous reports (Figure 1(a) and Supplementary Table S1) [25]. Initially, the N-terminal domain (R1) was thought to form a globular structure, while the other domains form coiled-coil rods. However, sequence analysis of rootletin suggested that R1 contains two separate coiled-coil regions (Figure 1(a)). We performed coimmunoprecipitation assays to determine the physical interactions among CCDs of rootletin. Ectopic rootletin fragments were tagged with either Flag or GFP and co-expressed in HEK293T cells. The results showed that R2, R3, and R4 had homotypic interactions, whereas R1 did not (Figure 1(b) and Supplementary Figure S1). Our observations are consistent with a previous report that employed yeast two-hybrid interaction assays [25]. We also observed weak heterotypic interactions among some rootletin domains (Figure 1(b) and Supplementary Figure S1), which might be important for the formation of the higher-order filamentous structure of rootletin.

We transiently expressed individual domains of rootletin in HeLa cells and determined their subcellular localization. The full-length rootletin formed filaments at the centrosome, whereas individual domains were distributed throughout the cytoplasm (Figure 1(c)). However, R3 was also detected at the centrosome as a dot, suggesting that R3 includes a specific sequence for centrosomal localization of rootletin (Figure 1(c)).

Rootletin is known to interact with C-NAP1 at the proximal ends of centrioles. In fact, rootletin is barely detectable at the centrosomes in C-NAP1-deleted cells [26–28]. To test whether R3 includes a binding site for C-NAP1, we determined centrosomal localization of ectopic R3 in the C-NAP1-depleted HeLa cells. Immunostaining analyses revealed that R3 was scarcely detected at the centrosomes of C-NAP1-depleted cells (Figure 1(d)). As a control group, R3 with the PACT (pericentrin-AKAP450 centrosomal targeting) domain (R3-P) was detected at the centrosome even in the C-NAP1-depleted cells (Figure 1(d)). These results suggest that R3 is essential for the interaction with C-NAP1 at the centrosome.

To define a minimal region of rootletin necessary for centrosomal localization, we generated smaller R3 fragments (Figure 1(e)). After a series of immunostaining analyses with the truncated R3 fragments, we identified 1254–1354 as a minimal region (hereafter named CCD3–6) required for centrosomal localization (Figure 1(e) and (f)). However, the CCD3–6 fragment itself was not located at the centrosome (Figure 1(e) and (f)). Additional residues at either the N-terminal or C-terminal end of CCD3–6 were necessary for centrosomal localization, suggesting that the CCD3–6 region is necessary but not sufficient for interaction with C-NAP1 at the centrosome.

R3 as a key domain for centrosomal localization and linkage

We generated the individual domain-deletion mutants of rootletin and transiently expressed them in rootletin-depleted HeLa cells (Figure 2(a)). The

Figure 1. Centrosomal localization of CCD3 fragments. (a) Four rootletin fragments are shown in the schematic diagram. The five differently colored boxes represent the predicted coiled-coil regions. The centrosomal localization of each ectopic rootletin fragment is summarized on the right. (b) Interactions among rootletin fragments are represented in the color-coded table. The individual co-immunoprecipitation results are shown in Supplementary Figure S1. (c) The GFP-tagged rootletin fragments were expressed in HeLa cells and subjected to immunostaining with antibodies specific to GFP and γ-tubulin. (d) The centrosomal localization of GFP-R3 was observed in C-Nap1-depleted HeLa cells. R3 with PACT (R3-P) was used as a control. The cells were co-immunostained with antibodies specific to C-NAP1, GFP, and γ-tubulin. The scale bar represents 10 μm. (e) A schematic diagram of the deletion fragments of CCD3 and a summary of their centrosomal localization are shown. Detailed construct information is listed in Supplementary Table S1. (f) The deletion fragments of CCD3 tagged with GFP were expressed in HeLa cells and subjected to immunostaining with antibodies specific to GFP and γ-tubulin. The scale bar represents 2 μm.

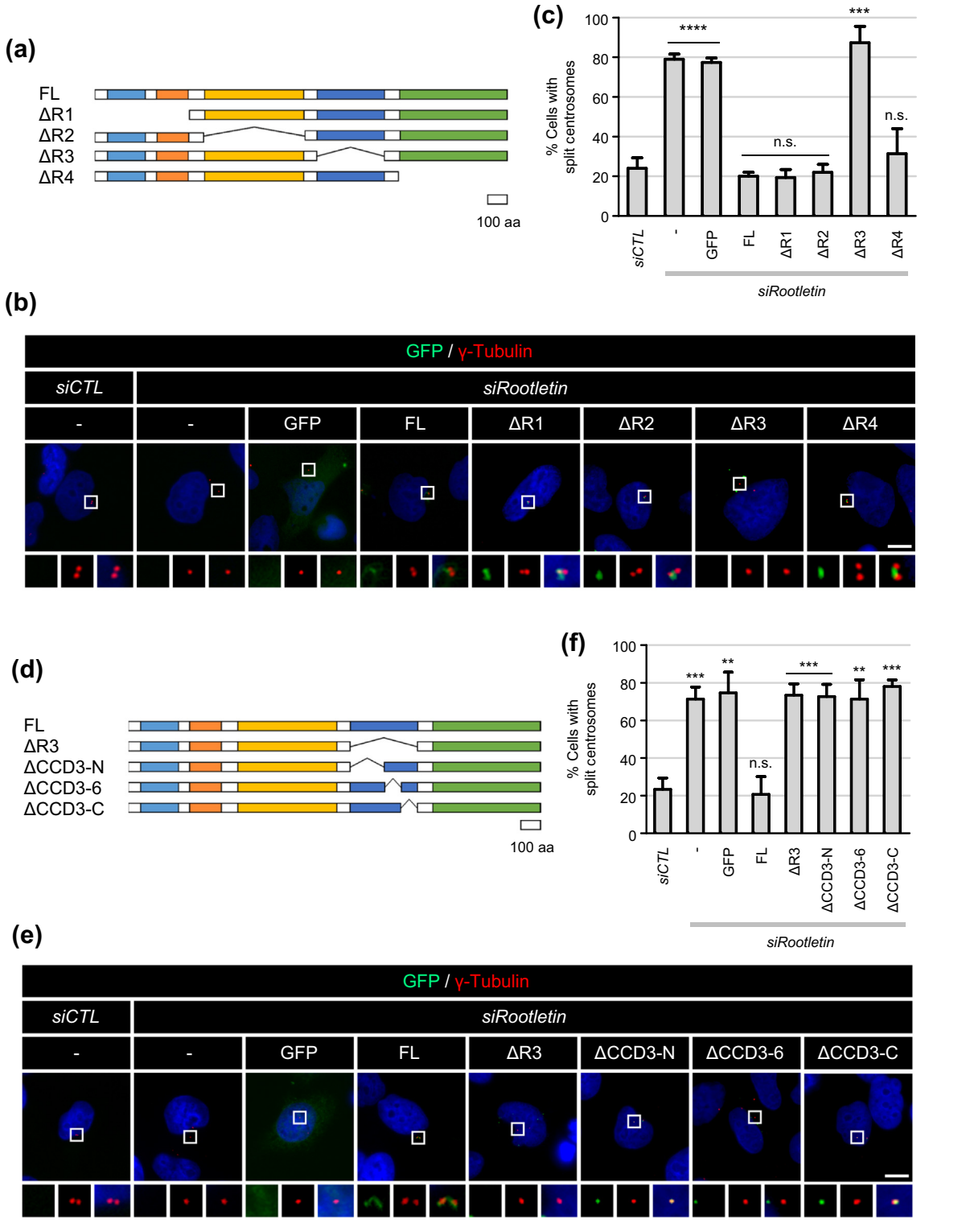

Figure 2. Requirement of R3 for centrosomal localization and centrosome cohesion. (a, d) A schematic diagram of the rootletin deletion mutants is presented. (b, e) The mutants were expressed in rootletin-depleted HeLa cells and subjected to immunostaining analysis with antibodies specific to GFP and γ-tubulin. The scale bar represents 10 μm. (c, f) The number of cells with split centrosomes was counted for each mutant, and the results are presented in a bar graph. More than 50 cells per experimental group were counted in three independent experiments. (**$P \leq .01$; ***$P \leq .001$; ****$P \leq .0001$; n.s.: not significant).

immunostaining analysis revealed that the ectopic rootletin mutants were located at the centrosomes, with the exception of rootletin$^{\Delta R3}$ (Figure 2(b)). Previously, depletion of rootletin was reported to increase the centrosome split in interphase cells [7]. We observed centrosome splitting in rootletin-depleted HeLa cells but this phenotype was rescued by expression of the full-length and deletion mutants of rootletin except for rootletin$^{\Delta R3}$ (Figure 2(c)). These results indicate that R3 is essential for both centrosomal localization and inter-centriole linkage. However, expression of the R3 fragment did not rescue the split centrosome phenotype in rootletin-depleted cells (Supplementary Figures S2 and S3).

We generated additional deletion mutants of rootletin in which parts of R3 were removed and transiently expressed them in rootletin-depleted HeLa cells (Figure 2(d)). The immunostaining analysis revealed that rootletin$^{\Delta R3\text{-}N}$ and rootletin$^{\Delta R3\text{-}C}$ were detected at the centrosome, but rootletin$^{\Delta CCD3\text{–}6}$ was not (Figure 2(e)). These results confirmed that CCD3–6 is the minimal region necessary for centrosomal localization. We also examined centrosome disjunction in the rootletin-depleted cells. The results showed that all the R3-deleted mutants failed to rescue the split centrosome phenotypes in rootletin-depleted interphase cells, indicating that an intact configuration of R3 is necessary for rootletin to assemble the inter-centriole linkage (Figure 2(f)).

Structural analysis of rootletin CCD3

As we showed that R3 is a critical domain of rootletin for centrosomal localization and inter-centriole linkage, we next analyzed the biophysical and structural properties of R3, especially its coiled-coil domain (CCD3; 1108–1442). Based on sequence analyses with PSIPRED [29] and PCOILS [30], CCD3 was predicted to comprise a continuous alpha-helix and to form a coiled-coil structure (Supplementary Figure S4a). We initially attempted to purify the whole CCD3 for crystallization but failed because of heterogeneous oligomer formation and degradation. To obtain a stable fragment for the structural study, we carried out limited proteolysis of CCD3 with trypsin (Supplementary Figure S4b). The N- and C-terminal boundaries of two stable fragments were identified through Edman sequencing and an approximation of their molecular weights on an SDS-PAGE gel. Based on these data, we constructed two stable fragments, CCD3$^{1108\text{–}1200}$ and CCD3$^{1108\text{–}1317}$ for expression and confirmed that both fragments were stable against trypsin digestion (Figure 3(a) and Supplementary Figure S4b).

The crystal structures of CCD3$^{1108\text{–}1200}$ and CCD3$^{1108\text{–}1317}$ were determined at 1.3 and 2.8 Å resolution, respectively (Supplementary Table S2). Both fragments formed parallel homodimers (Figure 3(b)). The short (CCD3$^{1108\text{–}1200}$) and long (CCD3$^{1108\text{–}1317}$) fragments reached approximately 120 and 300 Å in length, respectively (Figure 3(b)). CCD3$^{1108\text{–}1200}$ was crystallized in a space group of $C2_1$, containing one dimer in an asymmetric unit. In the case of CCD3$^{1108\text{–}1317}$, two dimers were assembled in an anti-parallel manner in an asymmetric unit of the P1 space group (Supplementary Figure S5). Even if the 1188–1200 region is not modeled into the structure of CCD3$^{1108\text{–}1200}$ because of the lack of electron density, this region is well defined in the structure of the longer fragment, CCD3$^{1108\text{–}1317}$. Given that the CCD3$^{1108\text{–}1200}$ fragment was designed based on limited trypsin digestion, the region near the 1200 residue would be relatively more flexible than the other coiled-coil regions. Structural comparison of three dimer molecules, one from the CCD3$^{1108\text{–}1200}$ structure and two from the CCD3$^{1108\text{–}1317}$ structure (hereafter named AB$^{1108\text{–}1317}$ and CD$^{1108\text{–}1317}$ dimers), through alignment of the C-terminal half of CCD3$^{1108\text{–}1200}$ demonstrated different helical bendings for each dimer, which might be due to crystal lattice contacts as well as the structural flexibility of the helix (Supplementary Figure S6a).

Structural analysis with TWISTER [31] showed that CCD3$^{1108\text{–}1317}$ forms a left-handed coiled-coil structure containing 28 heptad repeats and one hendecad repeat, an 11-residue unit (equivalent to the insertion of four residues called “the stutter” into one heptad repeat) (Figure 3(c)). In all three dimeric molecules, this hendecad repeat (1124–1134) forms a partially untwisted helical region, as demonstrated by the high value of coiled-coil pitch (Supplementary Figure S6b). The H1131 residues from the two protomers participate in π-stacking interactions to stabilize this region (Figure 3(b)). Previously, the stutter, which has been described in the structures of coil 1B and coil 2 of vimentin and coil 2 of the K5–K14 heterodimer, was shown to induce helical bending by forming an untwisted helical stretch [32,33]. In our structure, it is difficult to assess whether this hendecad repeat induces dramatic bending of the coiled-coil structure since it is located close to the N terminus. The functional implication of the non-heptad repeat was demonstrated by the fact that the loss of a stutter by the addition of three amino acids impairs the filament-forming ability of vimentin [34]. Moreover, the recently published structure of the coiled-coil NEMO dimer showed that its stutter region has a larger interhelical spacing, resulting in the structural flexibility of the coiled-coil dimer, which may facilitate the binding of IκB kinase (IKK)-β [35]. Sequence analysis of CCD3 showed another hendecad repeat appearing in the region 1359–1369 (Supplementary Figure S7). It is still unknown whether these hendecad repeats in rootletin have a functional significance in filament formation and/or protein–protein interaction.

CCD3$^{1108\text{–}1317}$ contains 28 heptad repeats, which generally have Leu and Val at the *a* and *d* positions

to stabilize the coiled-coil structure by forming a hydrophobic interaction network at the core. However, 7 out of 28 heptad repeats in CCD3$^{1108–1317}$ have Ala at the *a* and *d* positions (Figure 3(b) and (c)). A previous structural study on tropomyosin, which forms a coiled-coil dimer and binds to actin filaments, showed that Ala at the *a* and *d* positions of a heptad repeat can provide helical flexibility, and thus, helical bending occurs near this region [36,37]. The frequency of Ala or Gly at the *a* and *d* positions in CCD3 is much higher than in vimentin but similar to tropomyosin (Supplementary Figure S6c), suggesting that CCD3 has more structural flexibility than vimentin. While vimentin is part of the cytoskeletal

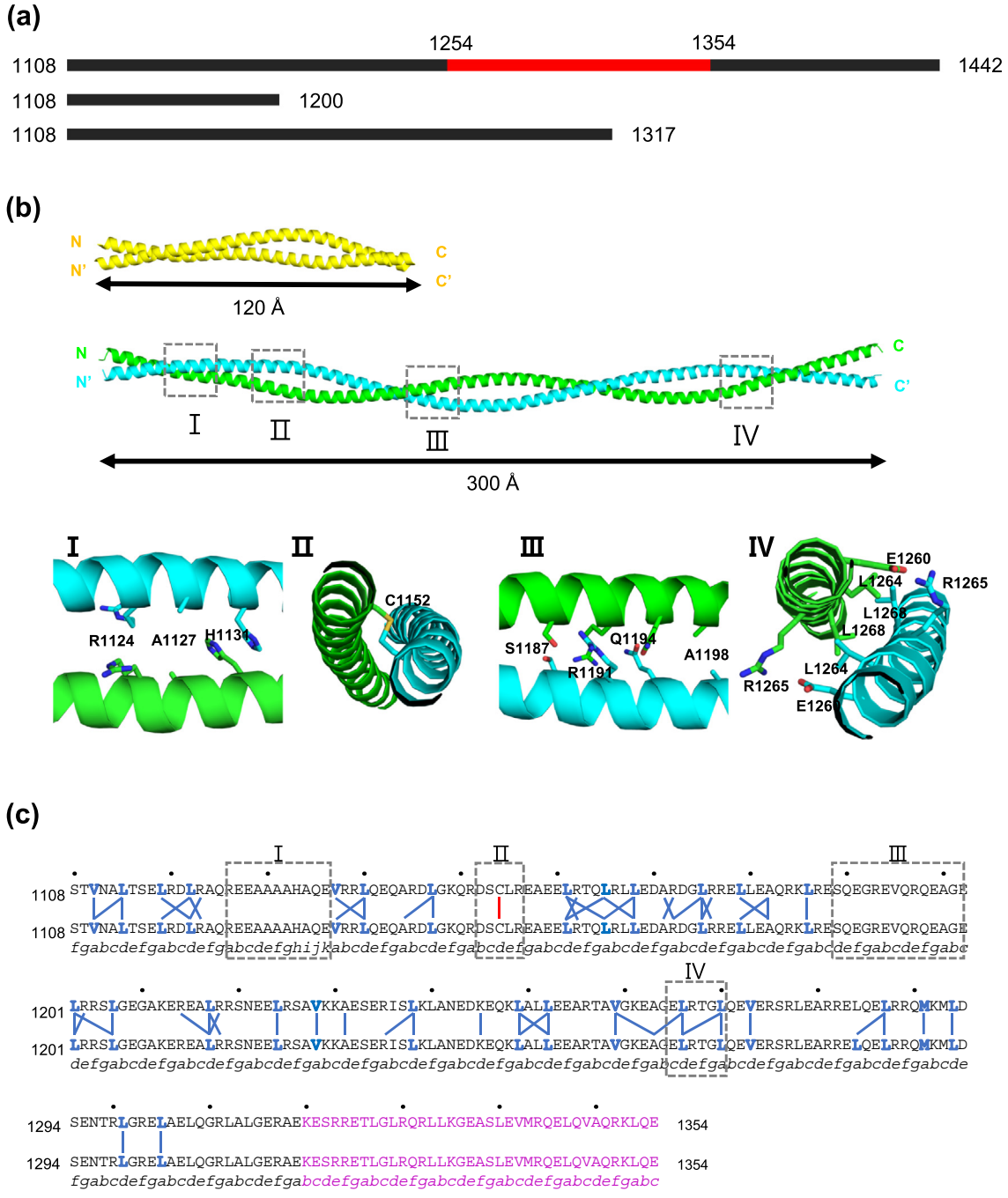

Figure 3 (*legend on next page*)

network to maintain cell integrity, rootletin as a centrosome linker, may require structural dynamics for its cellular function.

Two of the three CCD3 dimers ($CCD3^{1108–1200}$ and $AB^{1108–1317}$) contain disulfide bonds between two C1152 residues from each protomer (Figure 3(b)). This was unexpected because 1 mM TCEP (Tris [2-carboxyethyl] phosphine) was included as a reducing agent in the purification buffer and the crystallization solution. Structural comparison between the two dimers of $CCD3^{1108–1317}$ in the C1152 region showed that disulfide bond formation does not affect the overall helical structure but could enhance structural stability. In fact, disulfide bonds are observed in other centrosome proteins [38]. It is possible that the centrosome may be under an oxidative condition sufficient to form a disulfide bond [39].

Taken together, our structural analysis suggests that hydrophobic interactions and covalent bond formation contribute to the formation of a left-handed coiled-coil homodimer (Figure 3). In fact, we demonstrated that both hydrophobic core formation by Leu residues at the *a* and *d* positions and disulfide bond formation are important for stabilizing a coiled-coil dimer using the $CCD3^{1108–1354}$ mutant, in which 26 Leu and 1 Cys residues were substituted with Ser and Ala, respectively ($CCD3^{1108–1354\text{-}26LS}$ mutant) (Figure 4(a)). Multi-angle light scattering (MALS) analysis showed that $CCD3^{1108–1354\text{-}26LS}$ remained as monomers, whereas $CCD3^{1108–1354}$ formed dimers (Figure 4(b)). Moreover, crosslinking experiments with the BS^3 crosslinker showed that most $CCD3^{1108–1354\text{-}26LS}$ remained as monomers, and only a small fraction of them formed dimers (Figure 4(c)). On the other hand, most $CCD3^{1108–1354}$ formed dimers and multimers upon BS^3 treatment (Figure 4(c)). These results confirmed the importance of hydrophobic interactions for dimer formation and even multimer formation.

Biophysical analysis of rootletin fragment CCD3–6

As the CCD3–6 fragment appears to be functionally important according to our cell-based assays, we investigated its biophysical properties of the CCD3–6 fragment, part of which is not included in our structure. MALS analysis demonstrated that the purified CCD3–6 formed dimers in solution (Figure 5(a)). Please note that the N-terminal 60 amino acids of CCD3–6 are resolved as a coiled-coil dimer in our crystal structure of the long fragment. However, CCD3–6 was shown to have low thermal stability. Analysis with circular dichroism (CD) spectroscopy revealed that the melting temperature (Tm) of CCD3–6 was 37 °C, whereas that of $CCD3^{1108–1200}$ was 77 °C (Figure 5(b)). Such low thermal stability suggests that CCD3–6 may have a weak coiled-coil forming capacity. In the case of $CCD3^{1108–1354}$, which involves CCD3–6 in addition to our long fragment used for structure determination, two phases of the melting curve were observed with Tm values of 39 °C and 77 °C (Figure 5(b)). Furthermore, CCD3–6 was more sensitive to proteolytic digestion than $CCD3^{1108–1200}$ (Figure 5(c)). $CCD3^{1108–1200}$ has 19 potential trypsin cleavage sites, but they are not accessible to trypsin because of the formation of a stable coiled-coil structure. In contrast, CCD3–6, containing 23 Lys/Arg residues, is easily degraded by trypsin (Figure 5(c)). Coiled-coil prediction by PCOILS showed that coiled-coil breakage occurs in the 1313–1332 region (Supplementary Figure S4a). Indeed, if the heptad repeat continues, G1313 and E1317 would occupy the *d* and *a* positions, respectively, followed by S1320 at the *d* position (Figure 3(c)). Overall, the C-terminal 40 amino acids of CCD3–6 may not form a stable coiled-coil structure and likely adopts an open conformation exhibiting structural dynamics, as shown in the coil 1A segment of vimentin [31]. Accordingly, the helical content of CCD3–6 in solution measured by CD spectroscopy was approximately 55%, compared with the 75% in $CCD3^{1108–1200}$ (Supplementary Figure S8).

Characterization of the rootletin CCD3 oligomer

To determine the oligomeric status of CCD3–6 in solution, we carried out crosslinking experiments with the BS^3 crosslinker. In contrast to $CCD3^{1108–1200}$, most of which remained dimers on the SDS-PAGE gel

Figure 3. Crystal structures of rootletin CCD3 fragments. (a) Schematic view of CCD3 fragments used for proteolytic digestion (CCD3;1108–1442) and crystallization ($CCD3^{1108–1200}$ and $CCD3^{1108–1317}$) are shown. The red boxed region represents CCD3–6. (b) Crystal structures of $CCD3^{1108–1200}$ (yellow) and $CCD3^{1108–1317}$ (green and cyan) are shown as a ribbon diagram. Only one dimeric structure of $CCD3^{1108–1317}$ is presented (see Supplementary Figure S7). Four characteristic regions in the coiled-coil structure are boxed and zoomed below to show the dimeric interface in detail. Each boxed region shows the (i) π-stacking interaction between H1131 in the hendecad repeat region, (ii) disulfide bond formed by C1152, (iii) heptad repeat with non-Leu residues at the *a* and *d* positions (S1187 and Q1194), and (iv) coiled-coil structure stabilized by hydrophobic and ionic interactions. (c) The amino acid sequence of the rootletin fragment $CCD3^{1108–1354}$ is represented by a single letter code. Amino acids not included in the crystallization construct (1318–1354) are colored magenta. The phases of the heptad (*abcdefg*) and hendecad (*abcdefghijk*) repeats are described below the sequences. Hydrophobic residues (Leu, Met, and Val) located at the *a* and *d* positions and involved in hydrophobic interactions are marked in bold blue. The solid blue line represents a hydrophobic interaction between two protomers (within a distance of 4 Å), and the red line represents the disulfide bond. Dots on top of letters mark every tenth amino acid.

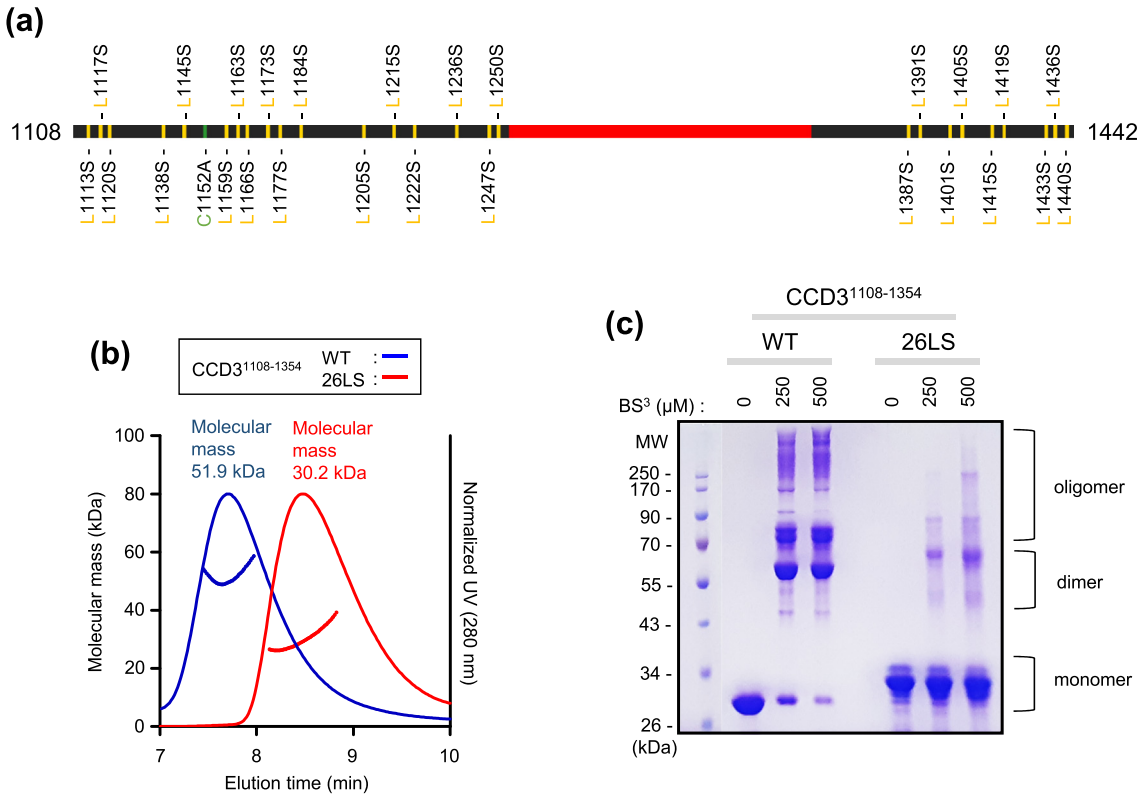

Figure 4. The importance of leucine residues for the dimerization of CCD3. (a) Mutation sites of the CCD3 LS mutant are shown. Twenty-six Leu residues and a Cys residue were substituted with Ser and Ala, respectively. The red region represents CCD3–6, which remains intact. (b) SEC-MALS analyses of the wild-type and LS mutant of CCD3$^{1108–1354}$ are presented. The calculated molecular mass of monomeric CCD3$^{1108–1354}$ is 29.2 kDa. Experimentally determined molecular weights are shown on top of each SEC profile. The molecular weight of wild-type CCD3$^{1108–1354}$ is close to the dimer size, and the molecular weight of the LS mutant is the monomer size. (c) The wild-type and 26 LS mutant of CCD3$^{1108–1354}$ were treated with the indicated amount of BS^3, and each reaction mixture was loaded onto an SDS-PAGE gel and visualized with Coomassie blue staining. Bands that shifted higher than dimer-sized bands are marked as oligomers.

after the crosslinking reaction, approximately half of CCD3–6 was not crosslinked, appearing as monomers on the SDS-PAGE gel, and the remaining half of CCD3–6 formed multimers as well as dimers (Figure 5(d)). These results support the notion that CCD3–6 shows conformational dynamics, existing in various oligomeric states ranging from monomers to higher-order oligomers. In fact, using size exclusion chromatography, we observed that purified CCD3–6 dimers were dissociated to monomers at concentrations lower than 100 μM (Supplementary Figure S9). On the other hand, at the same concentration, CCD3$^{1108–1200}$ stayed as a dimer. We also carried out crosslinking experiments with CCD3$^{1108–1354}$, which includes CCD3–6 and the ~140-amino-acid coiled-coil region at its N terminus. As expected, most of the CCD3$^{1108–1354}$ formed multimers as well as dimers (Figure 5(d)), whereas CCD3$^{1108–1317}$ did not form oligomers well. These results suggest that the structural dynamics of CCD3–6 play an important role in oligomer formation.

The CCD3 fragment had a low solubility and thus easily aggregated. Moreover, we noticed that the oligomeric state of CCD3 in solution varied from dimer to decamer, depending on the salt and protein concentrations. MALS analysis revealed that the purified CCD3 formed oligomers ranging from dimers to decamers under physiological salt conditions (150 mM NaCl) (Figure 6(a)). However, under high salt conditions, such as 500 mM NaCl, the molecular mass of CCD3 was measured as 350 kDa, corresponding to a decamer (Figure 6(a), Supplementary Figure S10). These observations suggest that oligomerization of the CCD3 dimers is mediated by hydrophobic interactions rather than ionic interactions because a high concentration of salts in solution is known to interfere with ionic interactions but to enhance hydrophobic interactions

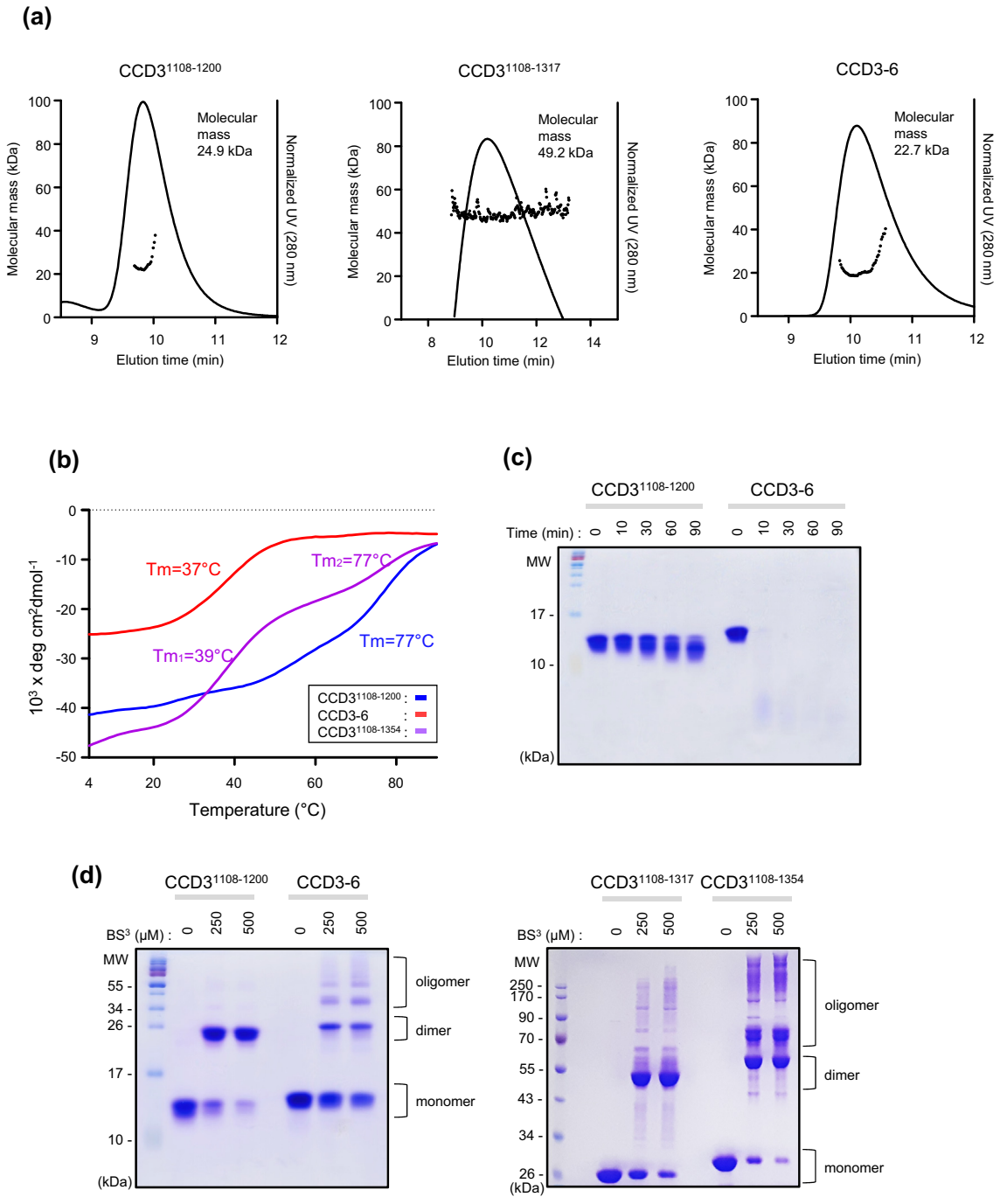

Figure 5. Biochemical analyses of the CCD3–6 fragment. (a) Normalized UV absorbance at 280 nm (right *y*-axis) and molecular weight (left *y*-axis) are plotted against the elution time of each CCD3 fragment. The measured molecular weights are displayed for each curve. The calculated molecular masses of each monomeric fragment based on its amino acid sequence are 11.4 kDa for CCD3$^{1108–1200}$, 24.8 kDa for CCD3$^{1108–1317}$, and 12.4 kDa for CCD3–6. (b) Thermal unfolding curves were measured by CD spectroscopy. CD spectra of CCD3–6 (red), CCD3$^{1108–1200}$ (blue), and CCD3$^{1108–1354}$ (purple) were recorded from 4 °C to 90 °C at 222 nm. The unfolding curve of 1108–1354 has two phases, with melting temperatures of 39 °C and 77 °C. (c) The structural stability of the rootletin fragments CCD3$^{1108–1200}$ and CCD3–6 was evaluated using a limited trypsin digestion experiment. Compared with CCD3$^{1108–1200}$, CCD3–6 was easily degraded. (d) Purified CCD3 fragments of rootletin (1108–1200, CCD3–6, 1108–1317, and 1108–1354) were treated with the indicated amount of BS^3, and each reaction mixture was loaded onto an SDS-PAGE gel. Bands that shifted higher than dimer-sized bands are marked as oligomers.

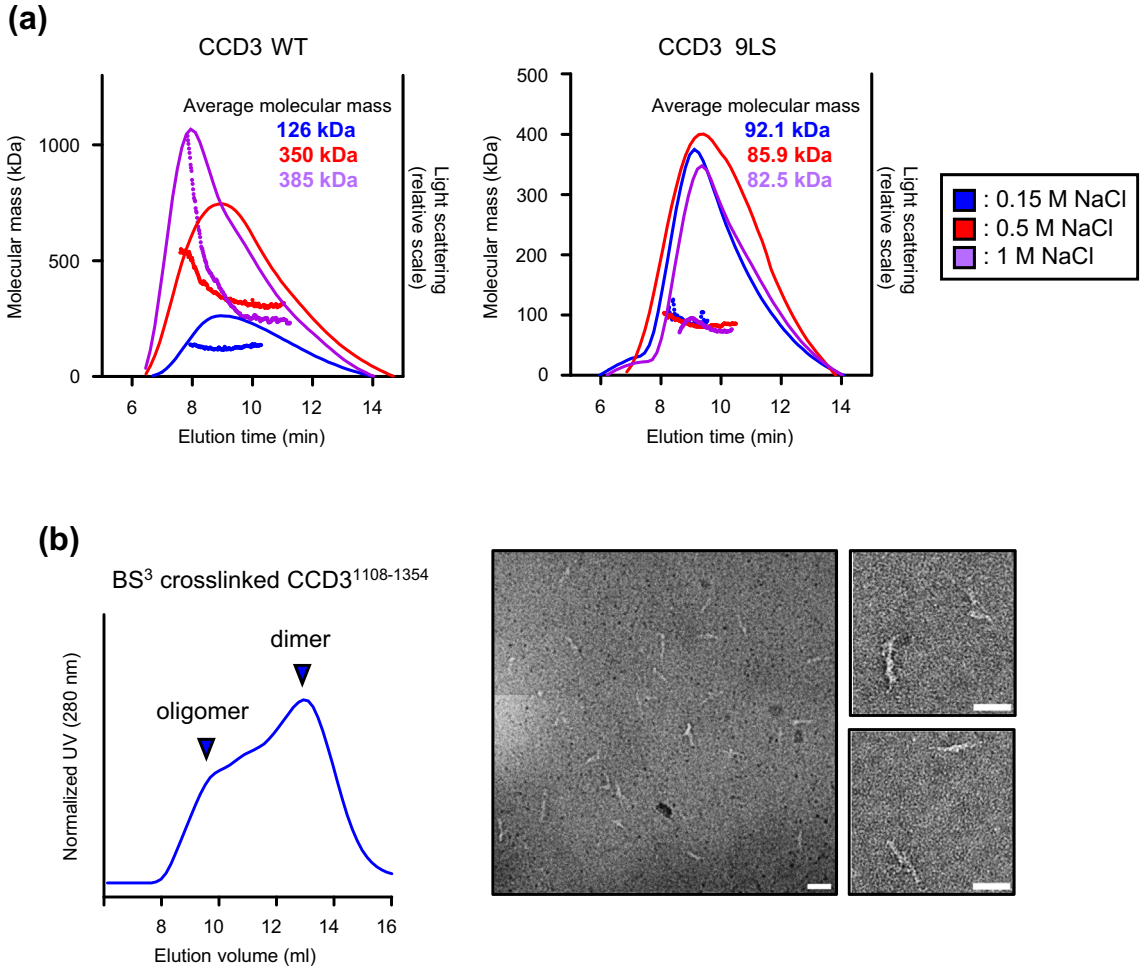

Figure 6. Oligomerization of CCD3. (a) SEC-MALS analyses of the wild-type and 9LS mutant of CCD3 were performed in buffers with different salt concentrations: 150 mM, 500 mM, and 1 M NaCl. SEC profiles of each sample in three different salt conditions are overlaid. Left and right axes show the molecular mass and light scattering signal, respectively. The molecular masses calculated from light scattering measurements are presented as horizontal lines and the weighted average molecular masses are shown. The calculated molecular mass of the CCD3 monomer based on the amino acid sequence is 38.9 kDa. (b) SEC profile of crosslinked $CCD3^{1108–1354}$ is shown on the left. Analytical gel filtration shows that crosslinking of $CCD3^{1108–1354}$ with BS^3 causes oligomerization of CCD3 dimers. A high molecular weight fraction from SEC, indicated by the blue arrow, was used to collect negative-stain EM images shown to the right. The length of each fiber is similar to that of the dimer based on the crystal structure, suggesting a lateral staggering mechanism of fiber formation for this fragment. The scale bar represents 40 nm.

at the protein interface. In fact, we noticed that some conserved Leu residues are positioned at the solvent-exposed regions (Supplementary Figure S7). These Leu residues on the surface are presumed to participate in hydrophobic interactions with neighboring molecules, thus stabilizing the oligomer. For example, direct contact between L1312 located at the *c* position of a heptad repeat in chain A and L1178 at the *b* position of a heptad repeat in chain C was observed at the dimer–dimer interface in our crystal structure (Supplementary Figure S5), although it remains unclear whether this direct interaction between antiparallel α-helical elements is physiologically relevant. To test our hypothesis that the Leu residues located at the outer surface mediate hydrophobic interactions with neighboring molecules, leading to oligomer formation, we generated a substitution mutant in which 9 Leu residues on the surface in the 1254–1442 region were substituted with Ser ($CCD3^{9LS}$) and determined its oligomeric states (Supplementary Figure S7). The results showed that, unlike CCD3, the $CCD3^{9LS}$ mutant formed a dimer, even under high salt conditions, supporting our hypothesis that CCD3 is oligomerized by hydrophobic interactions of Leu residues in the solvent-exposed region (Figure 6(a)).

The crosslinked CCD3 oligomers were observed using electron microscopy (EM). We fractionated

CCD3 using size exclusion chromatography and visualized the oligomer and dimer fractions with negative-staining EM. While the dimer sized fraction of CCD3 was too small to be detected by EM, oligomeric states of CCD3 were observed as filaments with an average length of approximately 40 nm, which is similar to the length of the predicted coiled-coil dimer based on our crystal structure (Figure 6(b)). This result supports the proposal that CCD3 oligomerizes by lateral staggering rather than head-to-tail elongation.

Role of rootletin oligomerization in its cellular function

We investigated the importance of the higher-order structure of rootletin using two CCD3 mutants: $CCD3^{1108–1354\text{-}26LS}$, which fails to form dimers, and $CCD3^{9LS}$, which fails to form higher-order oligomers in solution. We generated two stable cell lines in which $CCD3^{26LS}$ and $CCD3^{9LS}$ could be induced by doxycycline (Figure 7(a)) and performed immunostaining analyses. The results showed that neither $CCD3^{26LS}$ nor $CCD3^{9LS}$ was detected at the centrosome (Figure 7(b) and (c)). These results support the notion that stable coiled-coil dimer formation is a prerequisite for centrosomal localization of CCD3.

We generated two stable rootletin-depleted HeLa cell lines, each of which expresses GFP-rootletin containing the 26LS or 9LS substitutions of CCD3 (GFP-rootletin^{26LS} and GFP-rootletin^{9LS}) (Figure 8(a)). We confirmed that the ectopic rootletins were expressed in comparable amounts (Figure 8(b) and (c)). However, immunostaining analyses showed that both GFP-rootletin^{26LS} and GFP-rootletin^{9LS} were weakly detected at the centrosome as a dot (Figure 8(b)). Furthermore, we observed that both LS mutants failed to rescue centrosome disjunction in the rootletin-depleted cells (Figure 8(d)). These results suggest that dimerization and further oligomerization of CCD3 are essential for both centrosomal localization and inter-centrosome linkage.

Discussion

In this study, we performed biophysical and structural analyses of rootletin, a structural protein that constitutes ciliary rootlet and the inter-centriole linkage. We identified CCD3 as the key domain of rootletin by functional characterization, and then determined the crystal structures of the CCD3 fragments $CCD3^{1108–1200}$ and $CCD3^{1108–1317}$. The structures showed that both polypeptides formed parallel coiled-coil dimers. Hydrophobic interactions and a disulfide bond contribute to the formation of a stable homodimer, which was confirmed by the inability of a 26LS mutant to form a dimer. These results strongly suggest that the basic unit of rootletin is a parallel homodimer (Figure 9). Our results are consistent with the previously published yeast two-hybrid interaction assays [25].

Microscopic analysis of the rootlet filament revealed indented lines 75 nm apart, and the N-to-C distance between two rootletin molecules was estimated to be 35 to 40 nm [8]. Therefore, Schiebel and colleagues predicted that the rootlet filament may be arranged by staggering of parallel repeats of rootletin dimers [8]. Unfortunately, our structural analyses did not provide reliable clues suggesting how the rootletin dimers stagger to form a filamentous structure. Even if the tetrameric assembly of the $CCD3^{1108–1317}$ dimer in an antiparallel manner was observed in the asymmetric unit of the crystal lattice, it may not reflect the true configuration of the rootlet filament in cells. Nevertheless, we showed that the hydrophobic residues at the solvent-exposed region of the coiled-coil structure are important for oligomer formation.

We focused on the special biophysical properties of CCD3–6 necessary for the formation of higher-order oligomers. CCD3–6 is necessary for centrosomal localization of rootletin, suggesting that it contains a binding site for C-NAP1, which anchors the rootlet filament to the proximal end of the centriole. Furthermore, CCD3–6 is necessary for inter-centriole linkage formation, suggesting that it is essential for assembly of rootletin fibers. Even if we uncovered the functional importance of CCD3–6, our structural analysis was limited to the N-terminal half of CCD3–6 because of its flexibility and tendency to oligomerize. Limited proteolysis analysis suggests that the C-terminal region of CCD3–6 has structural flexibility.

The crystal structure of $CCD3^{1108–1317}$ showed that the N-terminal portion of CCD3–6 could form a homodimer within the context of a long coiled-coil structure. However, CCD3–6 itself may not form a stable coiled-coil dimer, since it exhibits low thermal stability with a Tm of 37 °C, whereas $CCD3^{1108–1200}$, an adjacent fragment with a similar size, has a Tm of 77 °C. Moreover, fluorescence-detection size exclusion chromatography (FSEC) analysis of serial dilutions of the CCD3–6 dimer showed that CCD3–6 forms a monomer at concentrations lower than 100 μM, while $CCD3^{1108–1200}$ remained as a dimer under the same conditions. These results suggest that CCD3–6 does not form a stable coiled-coil structure, and more likely, its C-terminal region forms an open conformation of an α-helix monomer or is completely disordered. In accordance with this idea, the CD spectroscopy analysis showed that the helical content of CCD3–6 was much lower than that of $CCD3^{1108–1200}$ (55% *versus* 75%). A similar biophysical property has been reported in coil 1A of vimentin, whose structure was determined to be a monomeric α-helix or was not resolved at all in the

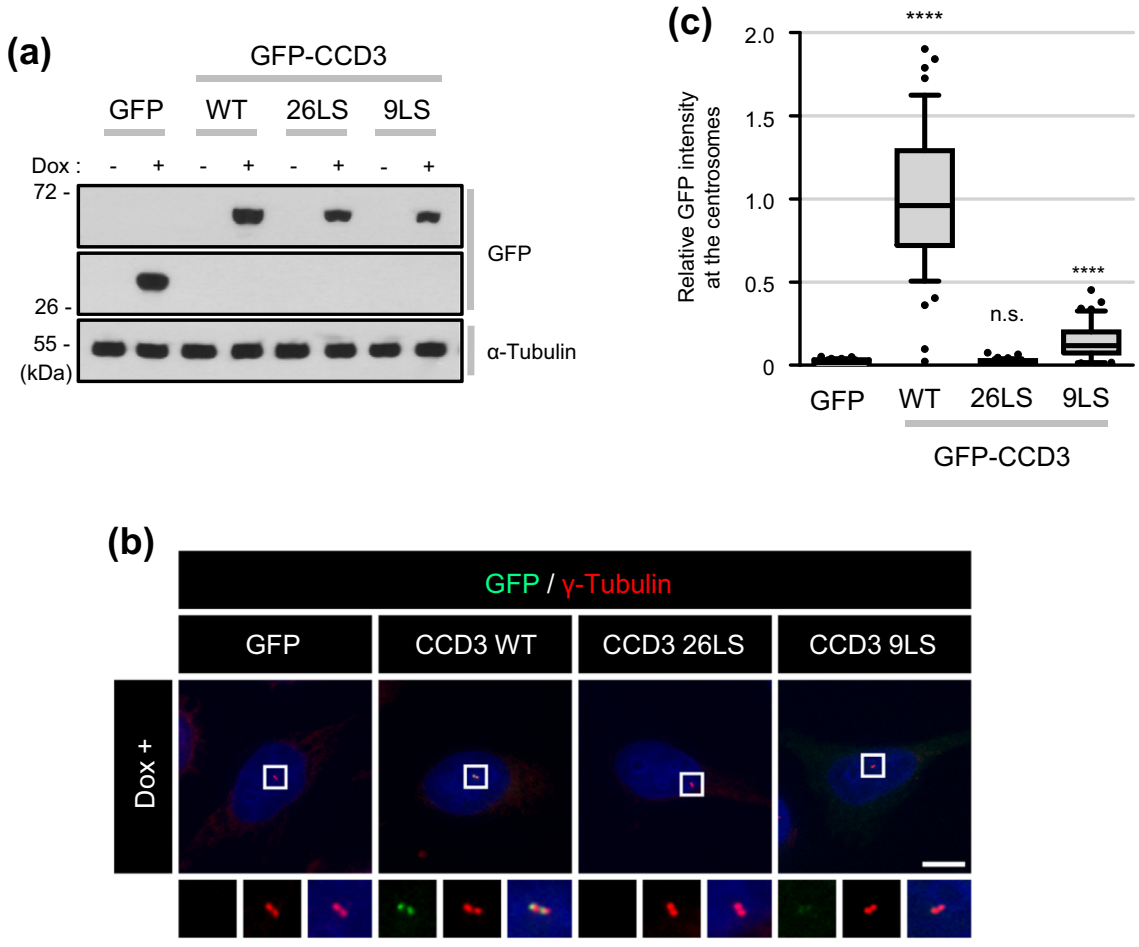

Figure 7. Importance of CCD3 oligomerization for centrosomal localization. (a) The rootletin mutants were expressed in HeLa-FRT/TO cells and subjected to immunoblot analyses with antibodies specific to rootletin, GFP, and α-tubulin. (b) The mutants were expressed in HeLa cells and subjected to co-immunostaining analysis with antibodies specific to GFP and γ-tubulin. The scale bar represents 10 μm. (c) The centrosomal intensities of the ectopic proteins were determined. More than 50 cells per experimental group were counted in three independent experiments. (****$P \leq .0001$; n.s.: not significant).

crystal structures [31,32]. Intriguingly, crosslinking analysis of CCD3–6 revealed that, although half of CCD3–6 appeared to stay as a monomer, a significant proportion of the remaining CCD3–6 formed multimers in solution. This result suggests that, despite the low tendency of CCD3–6 to dimerize on its own, once it forms a dimer, it readily assembles to form a higher-order oligomer. Thus, we propose that CCD3–6 functions as an oligomerization center (Figure 9). CCD3–6 may interact with the neighboring rootletin dimers for filament assembly and with C-NAP1 for centriole linkage. Similarly, the coil 1A fragment of vimentin was shown to be involved in intermediate filament assembly by forming a “cross-coil” with a neighboring coiled-coil dimer [40]. In addition, since CCD3–6 itself has structural instability, it should be stabilized by the adjacent domains, which form stable coiled-coil homodimers (Figure 9). This proposal is consistent with our observation that CCD3–6 requires additional sequences on either the N- or C-terminal side for its centrosome localization.

The oligomer formation of CCD3 was visualized by negative-stain EM analysis. Oligomerization of the purified CCD3 was demonstrated to thicken the fiber radius, not induce longitudinal elongation (Figure 6 (b)). Sequence analysis of CCD3 together with a surface model of our structure shows that, although charged residues are distributed at the solvent-exposed regions of the coiled-coil structure, prominent charged regions are not present, in contrast to the vimentin 1B dimer, which shows an evident acidic patch on the surface (Supplementary Figure S11) [25]. Therefore, it is reasonable to suggest that the major forces driving oligomer formation of CCD3 and vimentin are different. In the case of CCD3,

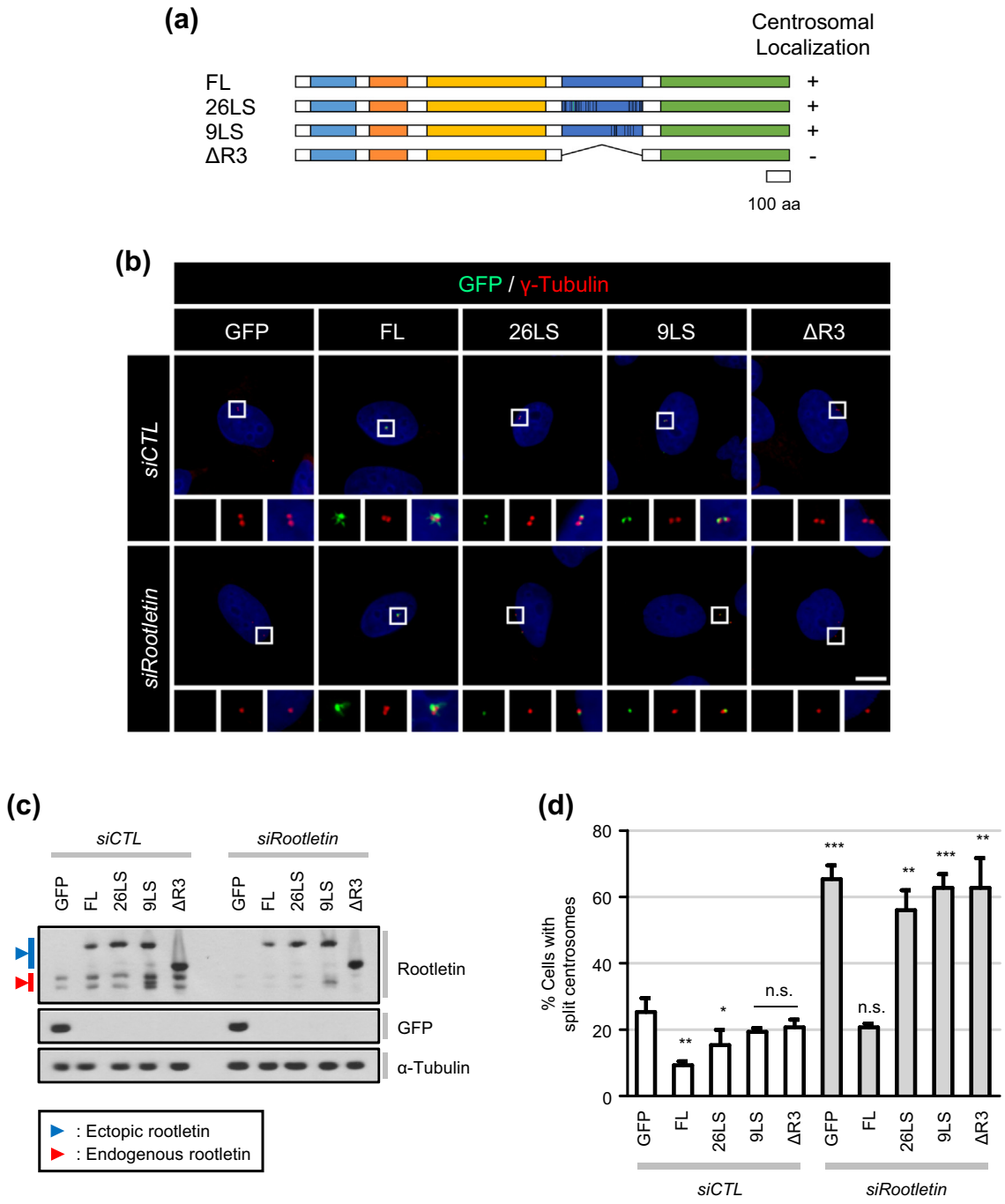

Figure 8. Importance of homophilic dimerization and oligomerization of CCD3 for centrosome cohesion. (a) Schematic diagram of the LS-substituted mutant and R3-deletion mutant of rootletin is shown. The 26 and 9 mutation sites in R3 are marked as lines (see Supplementary Figure 7 for details on mutation sites). The centrosomal localization of each rootletin mutant is summarized on the right. (b) The mutants were expressed in rootletin-depleted cells and subjected to co-immunostaining analysis with antibodies specific to GFP and γ-tubulin. The scale bar represents 10 μm. (c) Expression of the rootletin mutants in HeLa-FRT/TO cells was analyzed via immunoblot assays with antibodies specific to rootletin, GFP, and α-tubulin. (d) The number of cells with split centrosomes was determined. More than 50 cells per experimental group were counted in three independent experiments. (*$P \leq .05$; ***$P \leq .001$; n.s.: not significant).

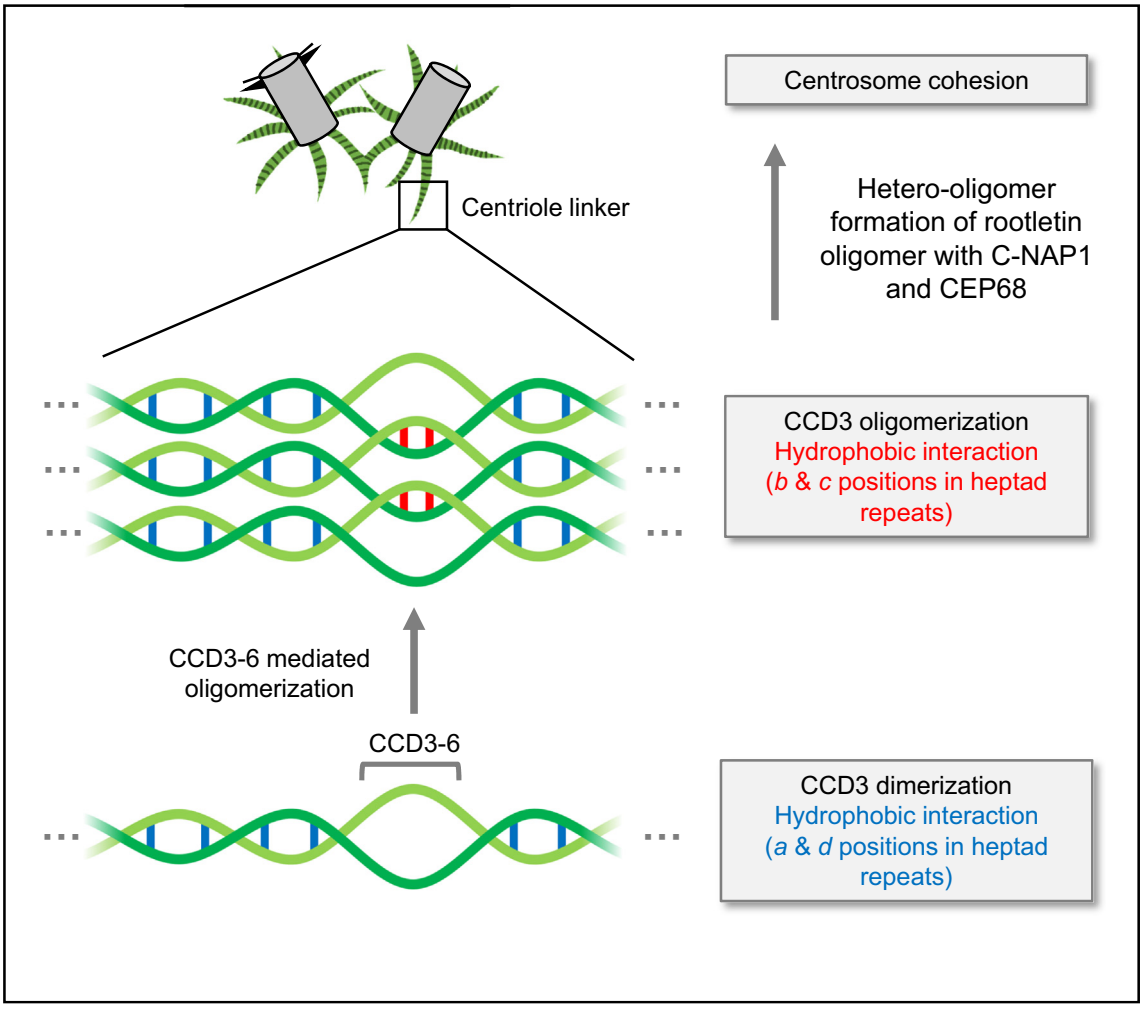

Figure 9. Assembly model of rootletin CCD3 fragments. A schematic drawing of lateral oligomerization of rootletin mediated by CCD3–6 is shown. Each protomer forming a rootletin dimer is colored dark and light green, respectively. Hydrophobic interactions mediated by hydrophobic residues at *a* and *d* positions in heptad repeats are represented in blue lines. They contribute to the formation of a stable coiled-coil dimer. Oligomerization of rootletin is mediated by CCD3–6, which could form "cross-coils" between adjacent coiled-coil dimers using hydrophobic residues in *b* and *c* positions in heptad repeats, represented in red lines. In the process of oligomerization of rootletin, C-NAP1 and CEP68 could be associated with form a hetero-oligomer. Once CCD3-mediated rootletin filaments are assembled, centrosome cohesion follows.

hydrophobic interactions, which were enforced under high salt conditions, are likely the major driving force of oligomerization. On the other hand, in many intermediate filament proteins, including vimentin, charged residues on the surface contribute to inter-molecular salt bridges that stabilize the filamentous states [41]. Altogether, we provide the molecular basis of CCD3 oligomerization using structural and biophysical analyses, along with a functional study. To understand the molecular mechanisms by which the fiber-like structure of rootletin is assembled and interacts with C-NAP1, further studies will be required on full-length rootletin and C-NAP1.

Materials and Methods

Antibodies and plasmids

Rabbit anti-rootletin (HPA021191; Sigma), mouse anti-GFP (sc-9996; Santa Cruz), rabbit anti-GFP (sc-8334; Santa Cruz), mouse anti-Flag (F3165; Sigma), mouse anti-alpha-tubulin (T6199; Sigma), mouse

anti-GAPDH (AM4300; Invitrogen), and goat anti-gamma-tubulin (sc-7396; Santa Cruz) antibodies were purchased from commercial suppliers. Alexa Fluor 488- and 594-conjugated secondary antibodies (Invitrogen) were used for immunostaining. Anti-mouse IgG-HRP (A9044; Sigma-Aldrich) and anti-rabbit IgG-HRP (AP132P; Millipore) were used as secondary antibodies for immunoblotting. The cDNA encoding full-length human rootletin was a gift form Erich A. Nigg, and it was subcloned into pEGFP-C1. Each rootletin mutant was subcloned into a pEGFP-C1 or 3xFlag-CMV10 vector. The siRNA-resistant constructs of rootletin were generated by site-directed mutagenesis. The PACT domain used in this study is the C-terminal region of the human pericentrin cDNA (9337–10,011 bp) [42]. LS mutations were made using gBlock gene synthesis (IDT).

Cell culture, transfection, and stable cell lines

HeLa and HEK293T cells were cultured in Dulbecco's modified Eagle's medium supplemented with 10% FBS at 37 °C under 5% CO_2. HeLa cells were transfected with the siRNAs using RNAiMAX (Invitrogen) and with the plasmids using Lipofectamine3000 (Invitrogen) according to the manufacturer's instructions. The siRNAs used in this study were siCTL (5′-GCA AUC GAA GCU CGG CUA CTT-3′), siRootletin (AAG CCA GUC UAG ACA AGG ATT-3′), and siC-Nap1 (5′-CUG GAA GAG CGU CUA ACU GAU TT-3′) [7]. To establish stable cell lines, rootletin and its mutants were subcloned into a pcDNA5 FRT/TO vector. For inducible expression, the HeLa Flp-In TREX cell line was transfected with the constructs using Lipofectamine3000 (Invitrogen), and stably transfected cell lines were selected with hygromycin (0.4 mg/ml) for approximately 2 weeks. To induce ectopic proteins, stable cell lines were treated with doxycycline (1 mg/ml).

Immunoprecipitation

For immunoprecipitation, HEK293T cells were transfected with DNA constructs using PEI. After transfection, the cells were lysed on ice for 20 min with a lysis buffer (50 mM Tris–HCl (pH 8.0), 5 mM EDTA, 150 mM NaCl, 0.5% Triton X-100, 1× protease inhibitor (P8340; Sigma-Aldrich), 0.5 mM PMSF, 1 mM DTT) [26]. After centrifugation at 12,000 rpm for 20 min, the supernatants were twice precleared by protein-A–Sepharose (GE Healthcare) for 1 h. Beads were then removed, and supernatants were incubated overnight with an antibody against GFP, followed by the addition of protein A–Sepharose for 1.5 h. Beads were washed three times with lysis buffer before SDS-PAGE and Western blotting analyses. All procedures were performed at 4 °C.

Immunocytochemistry and image processing

For immunocytochemistry, cells were cultured on 12-mm coverslips. The cells were fixed with cold methanol for 10 min, blocked with 3% BSA in 0.3% PBST (Triton X-100) for 20 min, incubated with primary antibodies for 1 h, and incubated with Alexa Fluor 488- and Alexa Fluor 594-conjugated secondary antibodies (Invitrogen). DAPI solution was used for DNA staining. The samples were mounted in ProLong Gold antifade reagent (P36930; Invitrogen) and observed using a fluorescence microscope (Olympus IX51) equipped with a CCD (QICAM Fast 1394, QImaging) camera. The images were analyzed using ImagePro 5.0 software (Media Cybernetics, Inc.). Statistical data were analyzed using SigmaPlot (Systat Software, Inc.).

Protein expression and purification

All rootletin constructs for structural and biochemical studies were designed to include His_6-MBP tags at their N terminus for affinity purification. For structure determination with Se-SAD/MAD (single-/multi-wavelength anomalous diffraction) phasing, Met residues were introduced into the rootletin constructs $CCD3^{1108–1200}$ and $CCD3^{1108–1317}$ by replacing L1153 and L1166, which are not conserved in other species. In *Mus musculus* rootletin, M1154 corresponds to L1153 of human rootletin (Supplementary Figure S7). To generate selenomethionyl-substituted proteins, expression constructs of $CCD3^{1108–1200}$ and $CCD3^{1108–1317}$ with L1153M and L1166M mutations ($CCD3^{1108–1200}$2LM, $CCD3^{1108–1317}$2LM) were transformed into the *Escherichia coli* methionine auxotrophic strain B834 (DE3). Transformed cells were grown in M9 medium supplemented with L-seleno-methionine at 37 °C until the OD_{600} reached 0.6. Protein expression was induced with 0.5 mM IPTG, and the cells were grown at 16 °C overnight. After cell harvest, the cell pellet was resuspended with phosphate-buffered saline (PBS; pH 7.4) supplemented with 5 mM 2-mercaptoethanol. Cells were lysed with emulsiflex C3 (Avestin) in the presence of 0.1 mM PMSF and DNase I (Roche). After centrifugation at 14,000 rpm for 30 min, cleared lysates were loaded onto a Ni-NTA column pre-equilibrated with 10 mM imidazole buffer (20 mM Tris–HCl (pH 8.0), 100 mM NaCl, 10 mM imidazole, 5 mM 2-mercaptoethanol). Bound proteins were eluted with a 250-mM imidazole buffer after extensive column washing with a 40-mM imidazole buffer. Eluted protein was treated with tobacco etch virus protease to cleave the His_6-MBP tag. Tagless rootletin fragments were separated from the uncleaved protein and the cleaved His_6-MBP tag using an amylose column and further purified by size exclusion chromatography (Superdex 200 10/300 GL, GE Healthcare) with a buffer consisting of 25 mM Tris–HCl (pH 8.0), 200 mM NaCl, and 1 mM TCEP.

For better purity of CCD3$^{1108–1317}$2LM, anion exchange chromatography (Hitrap Q HP, GE Healthcare) was performed before size exclusion chromatography.

Rootletins 1108–1200, 1108–1317, 1108–1354, and 1108–1442, as well as the LS mutants, were overexpressed in *E. coli* Rosetta (DE3) cells and purified similarly to Se-Met CCD3 as described above.

Crystallization, data collection, and structure determination

We initially screened the crystallization conditions with a Mosquito (TTP Labtech) crystallization robot using commercially available crystallization screening solutions on 96-well MRC plates. Initial hit conditions were further refined on 24-well linbro plates to obtain diffraction-quality crystals.

Se-Met crystals of CCD3$^{1108–1200}$2LM were obtained by equilibrating 2 µl of 5.3 mg/ml protein solution against mother liquor consisting of 150 mM sodium potassium tartrate and 16% PEG 3350 at 22 °C. Wild-type crystals were also obtained by the hanging-drop vapor diffusion method with a reservoir buffer consisting of 0.1 M Hepes (pH 7.0) and 14% PEG 4000. Wild-type crystals were cryoprotected with 15% glycerol in addition to mother liquor, and 2LM crystals were cryoprotected by increasing the PEG 3350 concentration of the mother liquor to 20%. A 1.3 Å resolution native and a 2.5 Å SAD data set were collected on the beamlines 5C and 11C at the Pohang Accelerator Laboratory (PAL, Korea).

From crystallization screening, Se-Met crystals of CCD3$^{1108–1317}$2LM were initially detected in a sitting drop equilibrated with a reservoir buffer containing 0.1 M Tris–HCl (pH 7.5) and 4% PEG 6000 at 5 °C. Multiple crystals grew within 1 day, and diffraction quality crystals were obtained by streak seeding. Crystals were cryoprotected with 20% ethylene glycol in addition to the mother liquor. A 2.8 Å resolution 3-wavelength MAD data set was collected on the beamline 5C at the Pohang Accelerator Laboratory (PAL, Korea).

All diffraction data sets were processed with the HKL2000 package [43] (Supplementary Table S2). Heavy atom search, phase calculation, and density modification were carried out using AutoSol program of the PHENIX package [44]. Cycles of manual rebuilding with the program COOT [45] and refinement with the programs PHENIX and BUSTER [46] were performed to generate the final models. Refinement statistics for each structure are shown in Supplementary Table S2.

CD spectroscopy

For CD spectroscopy, each protein sample was purified with PBS (pH 7.4) in which NaF and KF were present instead of NaCl and KCl to minimize the noise signal at 195 nm. CD spectra were obtained by scanning from 190 to 260 nm on a JASCO-815 spectrometer. To measure the melting temperature, CD data were measured at 222 nm by increasing the temperature from 4 °C to 90 °C with a continuous ramp rate of 1 °C/min. The secondary structure component was calculated using BESTSEL [47].

Size exclusion chromatography coupled with multi-angle light scattering

For determination of molecular mass, size exclusion chromatography coupled to multi-angle light scattering (SEC-MALS) was used. Each purified protein sample was concentrated to 1 to 5 mg/ml and applied to a Superdex 200 Increase 5/150 GL column (GE Healthcare) connected to MALS-UV-RI (refractive index) detectors (Wyatt TREOS). Protein concentration and the observed scattering signal were used to calculate the molecular mass with Zimm fit method (d*n*/d*c* value of 0.1850 ml/g) as implemented in Wyatt's ASTRA 7.14 software.

Crosslinking experiment and trypsin digestion assay

The crosslinking reaction was performed by incubating 0.2 mg/ml protein sample with the indicated amount of BS^3 crosslinker in PBS (pH 7.4) at room temperature for 10 min and was quenched with 50 mM Tris–HCl (pH 8.0) buffer. The reaction mixture was loaded on an SDS-PAGE gel to detect oligomerization status.

For limited proteolysis, the purified protein at a concentration of 0.4 mg/ml was mixed with 1 µg/ml trypsin (Thermo Fisher) dissolved in PBS (pH 7.4). Samples were taken at 10 and 90 min after incubation at room temperature and heated to stop the reaction. Each sample was loaded on an SDS-PAGE gel for visualization with Coomassie staining.

Negative-stain EM

After the crosslinking reaction of CCD3$^{1108–1354}$ with BS^3, the reaction mixture was loaded onto a Superdex200 column (GE Healthcare) pre-equilibrated with a buffer containing 25 mM Tris–HCl (pH 8.0) and 200 mM NaCl. Each fraction corresponding to dimeric and oligomeric states was applied to a glow-discharged carbon-coated EM grid (Cu-Mesh 200, EMS). The grids were blotted with filter paper, and 1% uranyl acetate was added for negative staining. EM images from each grid were obtained with a Tecnai G2 Spirit Twin transmission electron microscope (FEI Company, USA) operated at 120 kV using an Eagle (4K × 4K, FEI Company, USA) detector at a pixel size of 1.65 Å.

FSEC

Purified rootletin samples were diluted with size exclusion buffer (25 mM Tris–HCl (pH 8.0), 150 mM NaCl) at various concentrations (500, 100, and 50 μM), and a 25 μl sample was injected into a Superdex200 Increase 10/300 GL column. The fluorescence signal from tryptophan at the C terminus was detected by an FP-4025 fluorescence detector (JASCO) with a 280-nm excitation wavelength and 350-nm emission wavelength.

Accession numbers

The structure coordinates and structure factors have been deposited in the Protein Data Bank (PDB ID: 6L5H for Rootletin $^{1108–1200}$ and PDB ID: 6L5J for Rootletin $^{1108–1317}$).

Acknowledgments

This work was supported by Basic Research Laboratory Grant NRF-2014R1A4A10052590 (to K. R. and H.-J. C), Mid-Career Researcher Program NRF-2019R1A2C2002726 (to K. R.), and the Bio & Medical Technology Development Program NRF-2019M3E5D6063903 (to H.-J. C) of the National Research Foundation funded by the Korean government (MSIT). We thank beamlines 5C and 11C staffs at the Pohang Accelerator Laboratory for helping with the X-ray diffraction data collection. We thank Jinuk Kim (Seoul National University, Korea) for helping to obtain negative-stain EM images.

Author Contributions

D.K. performed cell-based studies, and J.K. carried out biochemical and structural studies. K.R. and H.-J.C. conceived and directed the study and wrote the manuscript with contributions from all authors.

Declaration of Competing Interest

The authors have no competing interests to declare.

Appendix A. Supplementary data

Supplementary data to this article can be found online at https://doi.org/10.1016/j.jmb.2020.04.012.

Received 6 January 2020;
Received in revised form 10 March 2020;
Accepted 13 April 2020
Available online 20 April 2020

Keywords:
centrosome;
rootletin;
coiled-coil structure;
structural dynamics;
C-NAP1

†D.K. and J.K. contributed equally to this work.

Abbreviations used:
CCD, coiled-coil domain; PCM, pericentriolar material; NEK2, NIMA (never in mitosis A)-related kinase2; STED microscopy, stimulated emission depletion microscopy; RPE, retinal pigmented epithelial; R1, 2, 3, and 4, rootletin fragment 1, 2, 3, and 4; GFP, green fluorescent protein; PACT domain, pericentrin-AKAP450 centrosomal targeting domain; SEC-MALS, size exclusion chromatography coupled with multi-angle light scattering; FSEC, fluorescence-detection size exclusion chromatography.

References

[1] M. Bettencourt-Dias, D.M. Glover, Centrosome biogenesis and function: centrosomics brings new understanding, Nat. Rev. Mol. Cell Biol. 8 (2007) 451–463.
[2] Stearns JLaT, Microtubule-organizing centres: a re-evaluation, Nat. Rev. Mol. Cell Biol. 8 (2007) 161–167.
[3] W.J. Wang, R.K. Soni, K. Uryu, M.F. Tsou, The conversion of centrioles to centrosomes: essential coupling of duplication with segregation, J. Cell Biol. 193 (2011) 727–739.
[4] E.A. Nigg, T. Stearns, The centrosome cycle: centriole biogenesis, duplication and inherent asymmetries, Nat. Cell Biol. 13 (2011) 1154–1160.
[5] G. Wang, Q. Jiang, C. Zhang, The role of mitotic kinases in coupling the centrosome cycle with the assembly of the mitotic spindle, J. Cell Sci. 127 (2014) 4111–4122.
[6] A.J. Faragher, A.M. Fry, Nek2A kinase stimulates centrosome disjunction and is required for formation of bipolar mitotic spindles, Mol. Biol. Cell 14 (2003) 2876–2889.
[7] S. Bahe, Y.D. Stierhof, C.J. Wilkinson, F. Leiss, E.A. Nigg, Rootletin forms centriole-associated filaments and functions in centrosome cohesion, J. Cell Biol. 171 (2005) 27–33.
[8] R. Vlijm, X. Li, M. Panic, D. Ruthnick, S. Hata, F. Herrmannsdorfer, et al., STED nanoscopy of the centrosome linker reveals a CEP68-organized, periodic rootletin network anchored to a C-Nap1 ring at centrioles, Proc. Natl. Acad. Sci. U. S. A. 115 (2018) E2246–E2253.
[9] S. Graser, Y.D. Stierhof, E.A. Nigg, Cep68 and Cep215 (Cdk5rap2) are required for centrosome cohesion, J. Cell Sci. 120 (2007) 4321–4331.
[10] G. Fang, D. Zhang, H. Yin, L. Zheng, X. Bi, L. Yuan, Centlein mediates an interaction between C-Nap1 and Cep68 to maintain centrosome cohesion, J. Cell Sci. 127 (2014) 1631–1639.
[11] Y. Xia, N. Huang, Z. Chen, F. Li, G. Fan, D. Ma, et al., CCDC102B functions in centrosome linker assembly and centrosome cohesion, J. Cell Sci. 131 (2018).

[12] R. He, N. Huang, Y. Bao, H. Zhou, J. Teng, J. Chen, LRRC45 is a centrosome linker component required for centrosome cohesion, Cell Rep. 4 (2013) 1100–1107.
[13] S. Bahmanyar, D.D. Kaplan, J.G. Deluca, T.H. Giddings Jr., E.T. O'Toole, M. Winey, et al., Beta-catenin is a Nek2 substrate involved in centrosome separation, Genes Dev. 22 (2008) 91–105.
[14] A.M. Fry, T. Mayor, P. Meraldi, Y.D. Stierhof, K. Tanaka, E.A. Nigg, C-Nap1, a novel centrosomal coiled-coil protein and candidate substrate of the cell cycle-regulated protein kinase Nek2, J. Cell Biol. 141 (1998) 1563–1574.
[15] A.M. Fry, R. Bayliss, J. Roig, Mitotic regulation by NEK kinase networks, Front Cell Dev. Biol. 5 (2017) 102.
[16] A.M. Fry, P. Meraldi, E.A. Nigg, A centrosomal function for the human Nek2 protein kinase, a member of the NIMA family of cell cycle regulators, EMBO J. 17 (1998) 470–481.
[17] T. Hardy, M. Lee, R.S. Hames, S.L. Prosser, D.M. Cheary, M. D. Samant, et al., Multisite phosphorylation of C-Nap1 releases it from Cep135 to trigger centrosome disjunction, J. Cell Sci. 127 (2014) 2493–2506.
[18] B.R. Mardin, M. Isokane, M.R. Cosenza, A. Kramer, J. Ellenberg, A.M. Fry, et al., EGF-induced centrosome separation promotes mitotic progression and cell survival, Dev. Cell 25 (2013) 229–240.
[19] A. Guemez-Gamboa, N.G. Coufal, J.G. Gleeson, Primary cilia in the developing and mature brain, Neuron. 82 (2014) 511–521.
[20] M.V. Nachury, D.U. Mick, Establishing and regulating the composition of cilia for signal transduction, Nat. Rev. Mol. Cell Biol. 20 (2019) 389–405.
[21] J. Yang, J. Gao, M. Adamian, X.H. Wen, B. Pawlyk, L. Zhang, et al., The ciliary rootlet maintains long-term stability of sensory cilia, Mol. Cell. Biol. 25 (2005) 4129–4137.
[22] J.V. Chen, L.R. Kao, S.C. Jana, E. Sivan-Loukianova, S. Mendonca, O.A. Cabrera, et al., Rootletin organizes the ciliary rootlet to achieve neuron sensory function in *Drosophila*, J. Cell Biol. 211 (2015) 435–453.
[23] K. Styczynska-Soczka, A.P. Jarman, The *Drosophila* homologue of Rootletin is required for mechanosensory function and ciliary rootlet formation in chordotonal sensory neurons, Cilia 4 (2015) 9.
[24] S. Mohan, T.A. Timbers, J. Kennedy, O.E. Blacque, M.R. Leroux, Striated rootlet and nonfilamentous forms of rootletin maintain ciliary function, Curr. Biol. 23 (2013) 2016–2022.
[25] J. Yang, X. Liu, G. Yue, M. Adamian, O. Bulgakov, T. Li, Rootletin, a novel coiled-coil protein, is a structural component of the ciliary rootlet, J. Cell Biol. 159 (2002) 431–440.
[26] J. Yang, M. Adamian, T. Li, Rootletin interacts with C-Nap1 and may function as a physical linker between the pair of centrioles/basal bodies in cells, Mol. Biol. Cell 17 (2006) 1033–1040.
[27] M. Panic, S. Hata, A. Neuner, E. Schiebel, The centrosomal linker and microtubules provide dual levels of spatial coordination of centrosomes, PLoS Genet. 11 (2015), e1005243.
[28] A.M. Flanagan, E. Stavenschi, S. Basavaraju, D. Gaboriau, D.A. Hoey, C.G. Morrison, Centriole splitting caused by loss of the centrosomal linker protein C-NAP1 reduces centriolar satellite density and impedes centrosome amplification, Mol. Biol. Cell 28 (2017) 736–745.
[29] D.W.A. Buchan, D.T. Jones, The PSIPRED Protein Analysis Workbench: 20 years on, Nucleic Acids Res. 47 (2019) W402–W407.
[30] L. Zimmermann, A. Stephens, S.Z. Nam, D. Rau, J. Kubler, M. Lozajic, et al., A completely reimplemented MPI bioinformatics toolkit with a new HHpred server at its core, J. Mol. Biol. 430 (2018) 2237–2243.
[31] S.V. Strelkov, P. Burkhard, Analysis of alpha-helical coiled coils with the program TWISTER reveals a structural mechanism for stutter compensation, J. Struct. Biol. 137 (2002) 54–64.
[32] A.A. Chernyatina, S. Nicolet, U. Aebi, H. Herrmann, S.V. Strelkov, Atomic structure of the vimentin central alpha-helical domain and its implications for intermediate filament assembly, Proc. Natl. Acad. Sci. U. S. A. 109 (2012) 13620–13625.
[33] C.H. Lee, M.S. Kim, B.M. Chung, D.J. Leahy, P.A. Coulombe, Structural basis for heteromeric assembly and perinuclear organization of keratin filaments, Nat. Struct. Mol. Biol. 19 (2012) 707–715.
[34] H. Herrmann, M. Haner, M. Brettel, N.O. Ku, U. Aebi, Characterization of distinct early assembly units of different intermediate filament proteins, J. Mol. Biol. 286 (1999) 1403–1420.
[35] A.H. Barczewski, M.J. Ragusa, D.F. Mierke, M. Pellegrini, The IKK-binding domain of NEMO is an irregular coiled coil with a dynamic binding interface, Sci. Rep. 9 (2019) 2950.
[36] J.H. Brown, Z. Zhou, L. Reshetnikova, H. Robinson, R.D. Yammani, L.S. Tobacman, et al., Structure of the mid-region of tropomyosin: bending and binding sites for actin, Proc. Natl. Acad. Sci. U. S. A. 102 (2005) 18878–18883.
[37] S. Minakata, K. Maeda, N. Oda, K. Wakabayashi, Y. Nitanai, Y. Maeda, Two-crystal structures of tropomyosin C-terminal fragment 176–273: exposure of the hydrophobic core to the solvent destabilizes the tropomyosin molecule, Biophys. J. 95 (2008) 710–719.
[38] Z. Feng, A. Caballe, A. Wainman, S. Johnson, A.F.M. Haensele, M.A. Cottee, et al., Structural basis for mitotic centrosome assembly in flies, Cell. 169 (2017) 1078–1089(e13).
[39] J.M. Lim, K.S. Lee, H.A. Woo, D. Kang, S.G. Rhee, Control of the pericentrosomal H_2O_2 level by peroxiredoxin I is critical for mitotic progression, J. Cell Biol. 210 (2015) 23–33.
[40] A. Premchandar, N. Mucke, J. Poznanski, T. Wedig, M. Kaus-Drobek, H. Herrmann, et al., Structural dynamics of the vimentin coiled-coil contact regions involved in filament assembly as revealed by hydrogen-deuterium exchange, J. Biol. Chem. 291 (2016) 24931–24950.
[41] D.A. Parry, P.M. Steinert, Intermediate filament structure, Curr. Opin. Cell Biol. 4 (1992) 94–98.
[42] A.K. Gillingham, S. Munro, The PACT domain, a conserved centrosomal targeting motif in the coiled-coil proteins AKAP450 and pericentrin, EMBO Rep. 1 (2000) 524–529.
[43] Z. Otwinowski, W. Minor, Processing of X-ray diffraction data collected in oscillation mode, Methods Enzymol. 276 (1997) 307–326.
[44] P.D. Adams, P.V. Afonine, G. Bunkoczi, V.B. Chen, I.W. Davis, N. Echols, et al., PHENIX: a comprehensive Python-based system for macromolecular structure solution, Acta Crystallogr. D Biol. Crystallogr. 66 (2010) 213–221.
[45] P. Emsley, B. Lohkamp, W.G. Scott, K. Cowtan, Features and development of Coot, Acta Crystallogr. D Biol. Crystallogr. 66 (2010) 486–501.
[46] G. Bricogne, E. Blanc, M. Brandl, C. Flensburg, P. Keller, W. Paciorek, et al., BUSTER Version 2.13.0, Global Phasing Ltd., Cambridge, United Kingdom, 2017.
[47] A. Micsonai, F. Wien, E. Bulyaki, J. Kun, E. Moussong, Y.H. Lee, et al., BeStSel: a web server for accurate protein secondary structure prediction and fold recognition from the circular dichroism spectra, Nucleic Acids Res. 46 (2018) W315–W322.